Energy materials

Sea urchin-like architectures and nanowire arrays of cobalt–manganese sulfides for superior electrochemical energy storage performance

Yuying Zhu[1] (iD), Haichao Chen[1,2,*] (iD), Si Chen[1] (iD), Chao Li[1] (iD), Meiqiang Fan[1] (iD), and Kangying Shu[1,*] (iD)

[1] College of Materials Science and Engineering, China Jiliang University (CJLU), Hangzhou 310018, China
[2] Institute of Materials for Energy and Environment, School of Materials Science and Engineering, Qingdao University, Qingdao 266071, China

ABSTRACT

Cobalt–manganese (Co–Mn)-based bimetallic compounds (such as Co–Mn oxides, hydroxides) have been investigated as a new type of high-performance electroactive materials for energy storage device. Nevertheless, Co–Mn sulfides are seldom investigated, especially for those with hierarchical architectures and structures. Herein, we first adopt a facile two-step hydrothermal route and synthesize Co–Mn sulfides with sea urchin-like architecture and nanowire array structure. The anion-exchange sulfuration process gives rise to hierarchical structure with numerous nanosheets grown on the surface. Benefiting from the attractive structures and the high electrochemical activity of Co–Mn sulfides, the Co–Mn sulfides show improved performance than Co–Mn oxides with similar morphology. Especially, the Ni foam-supported Co–Mn sulfide nanowire arrays exhibit superior performance of 502 C g^{-1} at 1 A g^{-1} as well as excellent cycling stability with 107% of capacity retention after 2000 cycles. In addition, a hybrid supercapacitor Co–Mn sulfide nanowire arrays/RGO displays an energy density of 18.4 Wh kg^{-1} at 375 W kg^{-1}. More importantly, an ultrahigh power density (22.5 kW kg^{-1} at 9.5 Wh kg^{-1}) and outstanding cycling stability can also be achieved. The excellent electrochemical performance can be ascribed to the attractive structure and high electrochemical activity of Co–Mn sulfide.

Introduction

Supercapacitors have received tremendous research attentions because of their high power density, rapid charging/discharging ability and long cycle life [1–4].

Such attractive properties make them the first-rank choice for applications requiring high power supply, such as electric vehicles, high-power electronic devices. Nevertheless, the widespread applications of supercapacitors, especially for the electric double-layer capacitors, are still restricted by their low

energy density (around 5 Wh kg^{-1}) in comparison with batteries which normally deliver more than 50 Wh kg^{-1} [1, 5]. So more research efforts should be focused on increasing the energy density of supercapacitor.

A successful attempt for better energy density has been conducted by replacing one supercapacitive electrode with a battery-type electrode, and such configuration is addressed as the hybrid supercapacitor. With the both contributions from its battery-type and capacitor-type electrodes, the hybrid supercapacitor shows an improved energy density while excellently maintaining the high-power performance of supercapacitor, and thereby demonstrates significant application potential [6–9]. As a typical battery-type material, binary transitional oxides, such as NiCo$_2$O$_4$ [10–12], NiFe$_2$O$_4$ [13] and ZnCo$_2$O$_4$ [14–16] have been wildly investigated owing to their higher specific capacity, excellent cycling stability than the monometallic oxides. In addition, Co–Mn oxides [17–19], such as Co$_x$Mn$_{3-x}$O$_4$, have been recently used as the electroactive materials for hybrid supercapacitors; it is found that cobalt element has higher intrinsic electric conductivity and superior rate performance [11, 20–24], while the manganese element involved can reduce the cost of electroactive material [25, 26]. More importantly, the Co ions and Mn ions can synergistic mutually improve the electrochemical performance, and thus show better electrochemical performance than single cobalt oxide or manganese oxide. For instance, Venkatachalam et al. [27] synthesized spinel structure MnCo$_2$O$_4$ nanorods and exhibit 287.5 C g^{-1} at 0.5 A g^{-1}. Zhang et al. [28] prepared Co$_{1.5}$Mn$_{1.5}$O$_4$ nanosheets with a high specific capacity of 307 C g^{-1} at 0.5 A g^{-1} as well as excellent cycling stability with no capacity decay after 1000 cycles. Peng et al. [29] reported that hierarchical core–shell CoMn$_2$O$_4$@-MnO$_2$ nanoneedle array demonstrates a specific capacitance of 2126 F g^{-1} at 1 A g^{-1}. Liu et al. [30] reported that Ni foam-supported manganese–cobalt oxysulfide shows a specific capacity of 490 C g^{-1} at 2 A g^{-1} and good rate performance of 415 C g^{-1} at 20 A g^{-1}. Those reports demonstrate the promising performance of Co–Mn-based compounds, but their electrochemical activity should be further improved to meet the need of practical application. Very recently, our research group has conducted a series of researches and found metal sulfides have better electrochemical activity than oxides [20, 31, 32]. More

attractively, our research group [33] found that a series of Co$_x$Mn$_{3-x}$ sulfides have excellent performance and the highest specific capacity of 289 C g^{-1} at 1 A g^{-1} has been attained for Co$_{2.5}$Mn$_{0.5}$ sulfide. Therefore, it is feasible to try Co–Mn sulfides as the electroactive materials for better electrochemical activity.

Additionally, to help the electroactive materials with high electrochemical utilization, especially at high rates, the electroactive materials should be exposed to the surface or near surface as much as possible. Therefore, morphology and structure are very important for electroactive materials. To date, a lot of reports have focused on designing the overall structure of electroactive materials, such as 3D architectures or arrays structures, to increase electroactive areas and facilitate the excellent contact with electrolyte [31, 32, 34–36]. Unfortunately, the microstructures have not paid sufficient attention despite they can greatly increase the electroactive areas of electroactive materials. For example, if a nanowire is porous or decorated with hierarchical structure on surface, the electroactive sites will be multiplied for energy storage. However, the microstructure designing has been usually omitted by researches because of the multistep synthesis process, which will bring extra cost and lengthy preparation process.

Herein, we develop a facile precursor-conversion method to synthesize Co–Mn sulfides with sea urchin-like architectures and nanowire arrays on Ni foam and used as electroactive materials for high-power energy storage. The exchanging of the Co–Mn precursor with S^{2-} generates attractive microstructure for the Co–Mn sulfides, and they become porous interiorly and grow nanosheets on the surface. Such a structure brings increased electroactive sites for energy storage and thereby achieves high electrochemical performance for high-power energy storage.

Experimental

Fabrication of Co–Mn precursor arrays on Ni foam and the urchin-like Co–Mn precursor

Firstly, a piece of Ni foam with a size of 2 × 4 cm was treated under ultrasonic washing successively with acetone to clean the surface and 3 M HCl to remove

oxide layer. Secondly, 7.5 mmol of $Co(NO_3)_2 \cdot 6H_2O$, 3.25 mmol of $Mn(NO_3)_2$ and 45 mmol of urea were dissolved into a mixed solution of 30 ml deionized water and 30 ml ethanol under magnetic stirring. After completely dissolved, the solution was transferred into an 80 ml Teflon-lined autoclave. Then, the Ni foam was put into the solution with a piece of polytetrafluoroethylene (PVDF) tape covered on one side. The autoclave was heated to 90 °C and maintained for 8 h, and the Co–Mn precursor on Ni foam can be harvested after washing with deionized water and ethanol. Meanwhile, the urchin-like precursor was also synthesized by same experimental procedure without adding the Ni foam substrate.

Fabrication of Co–Mn sulfide arrays on Ni foam and sea urchin-like Co–Mn sulfide

The Co–Mn sulfide arrays on Ni foam and sea urchin-like Co–Mn sulfide are prepared by reacting of the Co–Mn precursor with S^{2-}. Briefly, 0.4 g of $Na_2S \cdot 9H_2O$ was dissolved into 60 ml deionized water, and the Co–Mn precursor was added into the solution and treated under the hydrothermal condition at 160 °C for 6 h. The mass of Co–Mn sulfide on Ni foam was determined to be 2.9 mg cm^{-2} with precise weighting.

Fabrication of Co–Mn oxide arrays on Ni foam and sea urchin-like Co–Mn oxide

For comparison, the Co–Mn oxide arrays on Ni foam and sea urchin-like Co–Mn oxide have been synthesized by annealing the precursor at 280 °C for 3 h. The mass loading of Co–Mn oxide on Ni foam is $\sim$ 1.5 mg cm^{-2}, which is carefully determined by weighting the Ni foam before and after growing the Co–Mn oxide arrays.

Fabrication of reduced graphene oxide (RGO)

The RGO is prepared by reducing GO in the hydrothermal condition, and the details of experimental procedure can be found in our previous report [22, 31].

Materials characterization

X-ray diffraction (XRD, AXS D2 Phaser) was carried out to inspect the crystal structure of samples. Scanning electron microscope (SEM, HITACHI SU8010) and transmission electron microscope (TEM, JEM-2100) are used to observe the morphology and structure of samples. The SEM (HITACHI SU8010) equipped with EDX mapping test is used to characterize the compositions of sample. The elements near the surface of sample were examined by the X-ray photoelectron spectroscopy (XPS, Kratos, AXIS-ULTRA DLD-600 W) test. The elemental distribution was investigated by the SEM equipped with elemental mapping.

Electrochemical tests

The electrochemical measurements were conducted using a three-electrode system with 6 M KOH aqueous solution as electrolyte. A Pt foil (1 × 1 cm) and an Hg/HgO electrode are used as the counter electrode and reference electrode, respectively. As for the Co–Mn sulfide arrays and the Co–Mn oxide arrays, the Ni foam substrate can directly serve as the current collector and therefore the arrays were directly used as the working electrodes. With respect to the Co–Mn sulfide and Co–Mn oxide powder samples, the working electrodes were prepared by the following procedure: firstly, the active material, acetylene black and polytetrafluoroethylene with a mass ratio of 8:1:1 were added into ethanol solution and treated under ultrasonic condition for at least 1 h. After that, the mixture was dropped into Ni foam substrates ($d = 1.5$ cm) and kept in a hot air flow to evaporate the ethanol, and then dried at 60 °C for 10 h. Finally, the Ni foam was pressed at 10 MPa as the working electrode. The mass loading of active material on very Ni foam substrate is about 3 mg. Electrochemical tests were performed using a CHI660E workstation, the electrochemical performance of electroactive material was evaluated by the cyclic voltammetry (CV), galvanostatic charge–discharge test (GCD) and electrochemical impedance spectroscopy (EIS). The specific capacity values are calculated from the GCD curves according to the following equation [21, 24]:

$$C = \frac{It}{m} \tag{1}$$

where C (in C g^{-1}) is specific capacity; I is current; t is discharge time; and m represents the active material mass of the electrode.

The hybrid supercapacitor was fabricated using a two-electrode cell, and the Co–Mn sulfide electrode is used as the positive electrode, the capacitive RGO electrode is served as the negative electrode. The two electrodes were separated by a piece of hydrophilic separator. To balance the charge storage in each electrode, the mass ratio of two electrodes is determined by Eq. (2) as follows [24]:

$$\frac{m_+}{m_-} = \frac{C'_- V_-}{C_+} \tag{2}$$

where C (in C g^{-1}) is the specific capacity of the battery-type Co–Mn sulfide electrode, C' (in F g^{-1}) is the specific capacitance of capacitive RGO electrode and V is the potential window of the negative electrode. The energy density (E, in Wh kg^{-1}) and power density (P, in W kg^{-1}) of the hybrid supercapacitor are calculated from the GCD curves by the following equations, respectively:

$$E = \frac{1}{2 \times 3.6} C \Delta V \tag{3}$$

$$P = \frac{E \times 3600}{\Delta t} \tag{4}$$

where C is specific capacity of the hybrid device (in C g^{-1}); ΔV (V) is operating voltage window of the hybrid supercapacitor; and Δt (s) is discharge time.

Results and discussion

The typical process for fabricating the Co–Mn sulfides and oxides is illustrated in Fig. 1. The Co–Mn precursor is first prepared by the urea-assisted hydrothermal method. The Co(NO$_3$)$_2$·6H$_2$O and Mn(NO$_3$)$_2$ are used to produce Co^{2+} and Mn^{2+}, respectively; the urea serves as the precipitant and provides carbonate ions and alkaline environment for Co^{2+} and Mn^{2+} precipitation. The precursor is preferentially grown along the [100] direction [37], and thereby form the nanowire structure. Without the Ni foam substrate, the nanowires of precursor share a common center and extended radially outwards, giving rise to a sea urchin-like structure. When the Ni foam is added, the precursor can grow on its surface, forming a nanowire arrays structure. For the next step, the precursor is converted to the oxide and sulfide counterparts under annealing and hydrothermal conditions, respectively. The Co and Mn components in the precursor as well as the structure of precursor are well maintained, so Co–Mn oxides and sulfides with sea urchin-like structure and Ni foam-supported nanowire arrays structure have been harvested. The Co–Mn oxides are prepared by decomposing the precursor at high temperature without any motion of Co and Mn ions, so the Co–Mn oxides fully copy the morphology of precursor. The Co–Mn sulfides are synthesized by replacing the anions of the precursor with S^{2-}, which is happened

Figure 1 Schematic illustration of the fabrication process of sea urchin-like Co–Mn oxide and sulfide, and Ni foam-supported Co–Mn oxide and sulfide.
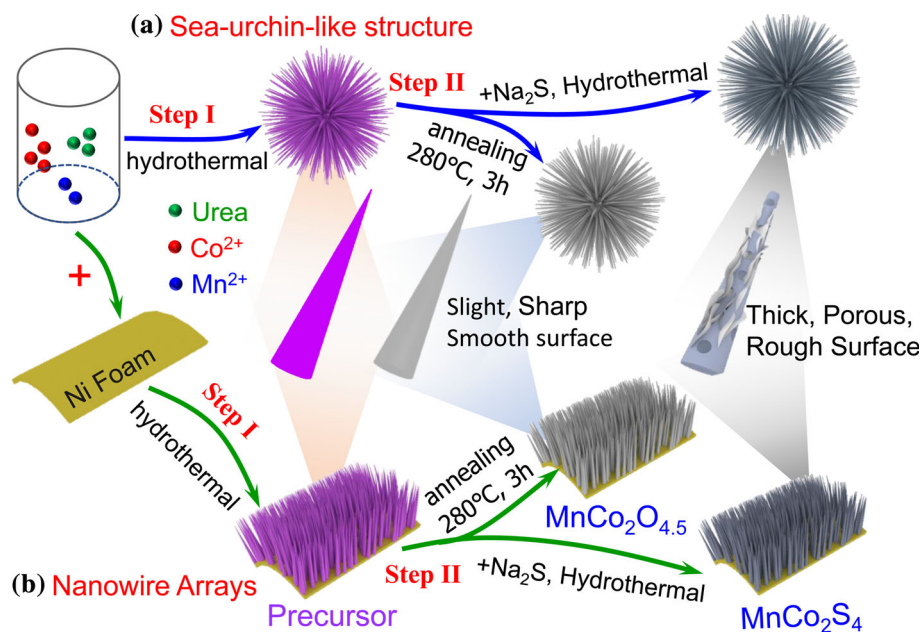
by the outer diffusion of Co and Mn ions and reacted with the S^{2-} in the solution, so the nanowires in the sea urchin-like structure and the Ni foam-supported arrays become much thicker with porous inside and rough surface. As the porous structure and the rough surface can enhance the electroactive sites for charge storage, and the porous structure is able to buffer the volumetric change that from repeat charging and discharging, such a structure feature of Co–Mn sulfides makes them potentially very promising for high-performance electroactive materials.

XRD measurement is used to characterize the crystal structure of Co–Mn-based precursors, oxides and sulfides with the results are shown in Fig. 2. For the sea urchin-like and Ni foam-supported Co–Mn sulfides, the diffraction peaks that located at 31.8°, 38.4°, 50.5° and 55.6° can be assigned to 311, 400, 511 and 440 planes of cubic phase of Co_3S_4 (JCPDS no. 02-0825). Besides of these diffraction peaks from Co_3S_4 phase, not any additional diffraction peak is observed, suggesting Mn ions substitute the Co ions in cubic Co_3S_4 phase without changing the crystal structure. With respect to Co–Mn precursors, the XRD peaks can be fully indexed to $Co(CO_3)_{0.5}$ $OH \cdot 0.11H_2O$ (JCPDS no. 48-0083), demonstrating synthesis of $Mn_{0.33}Co_{0.67}(CO_3)_{0.5}OH \cdot 0.11H_2O$. Therefore, the Co–Mn sulfides are synthesized by replacing the anions of precursor by S^{2-}. As for the annealing-treated samples, all the XRD peaks of both sea urchin-like and Ni foam-supported samples can be assigned to $MnCo_2O_{4.5}$ (JCPDS no. 32-0297),
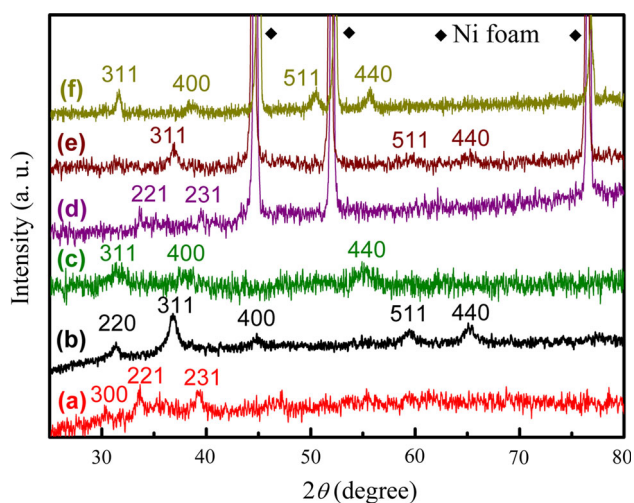

Figure 2 XRD patterns of sea urchin-like and Ni foam-supported (a, d) precursors, (b, e) Co–Mn oxides and (c, f) Co–Mn sulfides. (a–c) Sea urchin-like samples, (d–f) Ni foam-supported samples.

signifying the decomposition and transformation of precursors to oxides because of the annealing treatment.

In addition, both of the sea urchin-like and Ni foam-supported Co–Mn sulfides are measured by XPS test to investigate the surface chemical component and chemical states of each element. The sea urchin-like Co–Mn sulfide is directly used for XPS measurement, and the Ni foam-supported Co–Mn sulfide is first scraped from Ni foam and then used for XPS measurement. Figure 3a shows the survey spectra of the Co–Mn sulfides. The XPS peaks from Co, Mn, S and O can be obviously observed, which is indicative of the surface compositions are Co, Mn, S and O. The O may from the surface oxygen-containing functional group. For the Ni foam-supported Co–Mn sulfide, the XPS peak from Ni is also found because the violent scrap process unavoidable to destroy Ni foam surface. High magnified XPS spectra of Co, Mn and S compositions are also tested and analyzed, as shown in Fig. 3b–d. The Co 2p spectrum can be best fitted with two spin–orbit doublets together with two shake-up satellites (identified as Sat.), as shown in Fig. 3b. The peaks located at 776.48 and 793.48 eV are attributed to Co^{3+}, and the peaks at 781.38 and 797.07 eV are assigned to Co^{2+} [21, 22, 24]. The two main peaks of Mn 2p at 654.4 and 642.37 eV correspond to Mn $2p_{1/2}$ and Mn $2p_{3/2}$, respectively (Fig. 3c). The Mn $2p_{3/2}$ spectrum can be best fitted with two peaks at 645.6 eV and 642.5 eV, which confirms the existence of both Mn^{2+} and Mn^{3+} [38]. The main peaks of S 2p spectrum located at 162.0 and 163.3 eV belong to S $2p_{3/2}$ and S $2p_{1/2}$, respectively (Fig. 3d), which is the typical characteristic of sulfur ions with mental ions (Co–S and Mn–S bonding) [20, 22]. In addition, an extra peak at 168.6 eV can be observed, and such a peak is attributed to surface sulfur with high oxide state such as metal sulfates, which can be observed in the XPS spectrum of metal sulfide [34]. Thusly, the near-surface components of sample are Mn^{2+}, Mn^{3+}, Co^{2+}, Co^{3+} and S^{2-} according to the XPS spectrum analysis, which matches well with the Co–Mn sulfide.

The morphology and structure of sea urchin-like Co–Mn-based samples are characterized by SEM and TEM measurements. The precursor determines the main structure of the Co–Mn oxide and sulfide. As shown in Fig. 4a–d, the Co–Mn oxide and sulfide show a similar sea urchin-like structure compared to the precursor (Fig. S1). However, the different
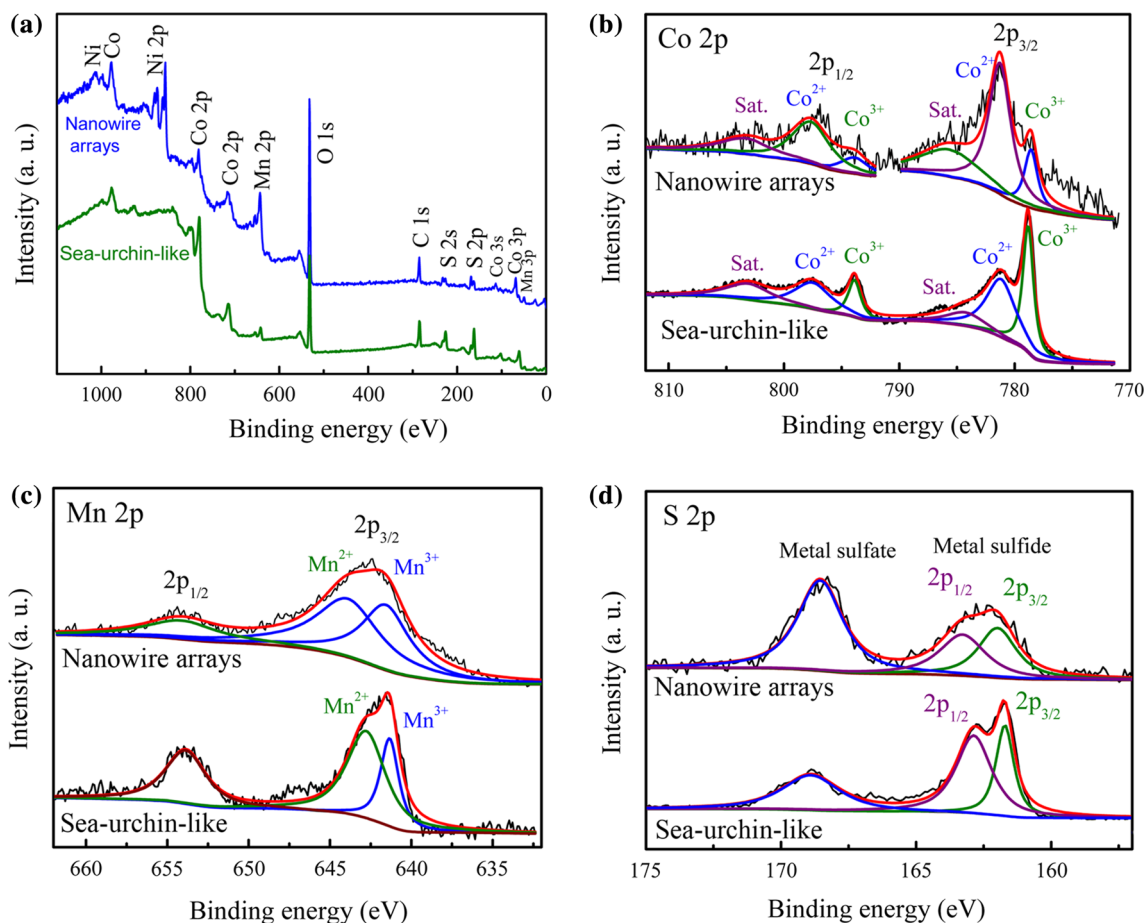
Figure 3 XPS spectra of **a** survey spectra, **b** Co 2p, **c** Mn 2p and **d** S 2p of sea urchin-like and Ni foam-supported Co–Mn sulfides. The Ni foam-supported sample is scraped from Ni foam for XPS test.

conversion condition also gives rise to varied microstructures for the sea urchin-like Co–Mn-based samples. For the Co–Mn oxide, the precursor only experiences a decomposition process without the motion of Co and Mn ions, so even the microstructure of the sea urchin-like precursor can be kept for the Co–Mn oxide. However, the precursor experiences an anion-exchange process and converts to Co–Mn sulfide. The inner Co and Mn ions of the nanowires cannot contact with S^{2-} unless they diffuse to the outer surface, so the metallic compositions are recombined with S^{2-} and thereby form the Co–Mn sulfide. Despite the sea urchin-like structure can still be maintained, some newly formed microstructure can be observed. As demonstrated by the TEM images in Fig. 4e, f, the nanowires in the sea urchin-like structure become porous with a rough surface, which can be attributed to the outer diffusion of Co and Mn ions in the anion-exchange process.

The Ni foam-supported Co–Mn nanowire arrays were also characterized by SEM and TEM measurements, as shown in Fig. 5. There is a uniform cover of nanowire arrays on Ni foam surface for the Co–Mn oxide and sulfide, and it is obvious that they have well maintained the nanowire arrays structure. The nanowires in the Co–Mn oxide arrays show a smooth surface, but they become much rough for the Co–Mn sulfide nanowires, so outer motion of Co and Mn ions happens when converting the precursor to Co–Mn sulfide. With an enlarge view, it is observed that Co–Mn sulfide nanowires become porous and their surfaces decorate numerous wrinkle layers (Fig. 5e, f). Such a structure is obviously able to greatly increase the electroactive sites and promote the excellent contact of the electroactive material with the electrolyte for better electrochemical performance. The elemental mapping that equipped in SEM has been used to characterize the compositions of Ni foam-supported Co–Mn sulfides, which demonstrates
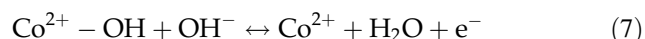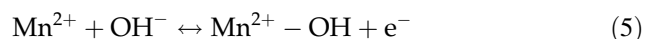
Figure 4 a, b SEM images of sea urchin-like Co–Mn oxide; **c, d** SEM and **e, f** TEM images of sea urchin-like Co–Mn sulfide.
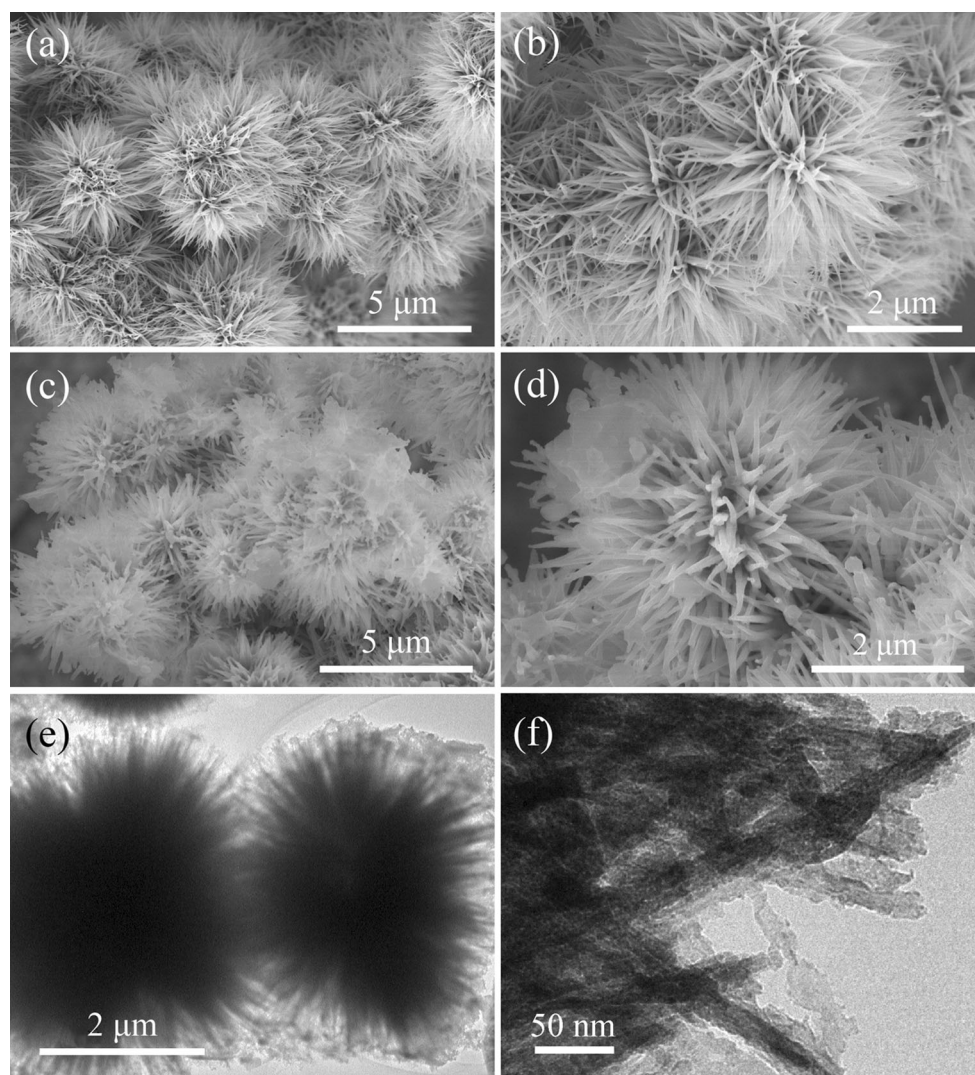
uniform distribution of Co, Mn and S elements, as shown in Fig. 5g. In addition, the sample has been characterized by selected area electron diffraction (SAED) test. As shown in Fig. 5h, the well-defined diffraction rings are indicative of polycrystalline nature of Co–Mn sulfide. The diffraction rings can be indexed to 311 and 440 planes of Co_3S_4 phase, which is in good agreement with the XRD result.

The electrochemical performance of the sea urchin-like Co–Mn oxide and sulfide, and the Ni foam-supported Co–Mn oxide and sulfide nanowire arrays are measured using the three-electrode method in aqueous and alkaline electrolyte. Figure 6a shows the CV curves of those Co–Mn-based electroactive materials at a scan rate of 5 mV s^{-1}. All the CV curves demonstrate obvious redox peaks, indicating their Faradaic properties. The redox peaks are from

the chemical reactions of Mn^{2+}/Mn^{3+}, Co^{2+}/Co^{3+} and Co^{3+}/Co^{4+} coming from the following reactions [39, 40]:

$$Mn^{2+} + OH^- \leftrightarrow Mn^{2+} - OH + e^- \tag{5}$$

$$Co^{2+} + OH^- \leftrightarrow Co^{2+} - OH + e^- \tag{6}$$

$$Co^{2+} - OH + OH^- \leftrightarrow Co^{2+} + H_2O + e^- \tag{7}$$

From Fig. 6a, it is found that the Co–Mn sulfide samples show vaguer and smaller redox peak separations than the Co–Mn oxide samples, demonstrating lower structure variation of electroactive materials while charging and discharging. As demonstrated by the SEM and TEM images in Figs. 4 and 5, the Co–Mn sulfides become very porous with numerous wrinkle layers decorated on the surface, so more electroactive materials locate on the surface or
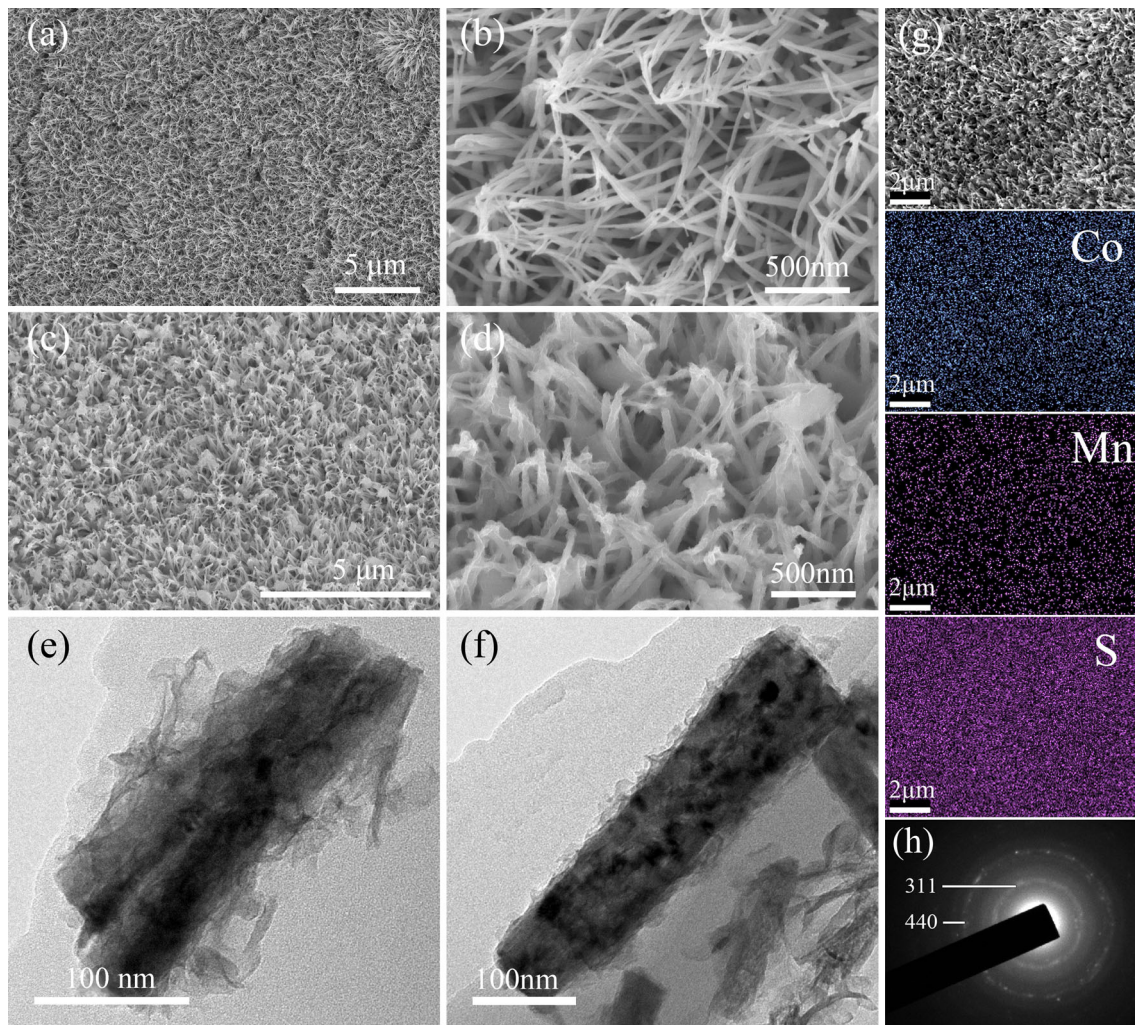
Figure 5 **a**, **b** SEM images of Co–Mn oxide arrays on Ni foam. **c**, **d** SEM and **e**, **f** TEM images of the Co–Mn sulfide arrays on Ni foam. **g** The elemental mapping images for Co, Mn and S elements and **h** SAED pattern of Ni foam-supported Co–Mn sulfide arrays.

near-surface range, and thereby leading to Co–Mn sulfide shows part of capacitive-like behavior. By comparing the CV curves, it is obvious that their integral areas greatly varied for different Co–Mn-based samples. As shown in Fig. 6a, the Ni foam-supported Co–Mn sulfide nanowire arrays demonstrate the highest capability for charge storage because of its largest CV integral area. The contribution from Ni is ignorable (Fig. S3), so the charge is mainly stored by Co–Mn sulfide. Figure 6b shows the GCD curves at 1 A g^{-1} of the Co–Mn-based samples, the longest charge and discharge time of the Ni foam-supported Co–Mn sulfide can further demonstrate the best electrochemical performance, which is in good agreement with the CV measurement.

Figure 6c, d, respectively, displays the CV and GCD curves at different rates of the Ni foam-

supported Co–Mn sulfide nanowire arrays (the CV and GCD curves of other three samples can be found in Fig. S2). As the rates increasing, the Co–Mn sulfide nanowire arrays maintain similar CV curve with low position shift of redox peaks and low IR drop in the GCD curves, signifying a rapid charge and discharge kinetic property. For better evaluating the electrochemical performance of Co–Mn-based samples, the specific capacity values are calculated from the GCD curves, which are plotted together in Fig. 6e for a fair comparison. There is a general trend that the Co–Mn sulfide demonstrates superior electrochemical performance than the Co–Mn oxide when they are prepared into similar morphology. The Ni foam-supported Co–Mn sulfide nanowire arrays and the sea urchin-like Co–Mn sulfide show much higher specific capacity values than Ni foam-supported Co–
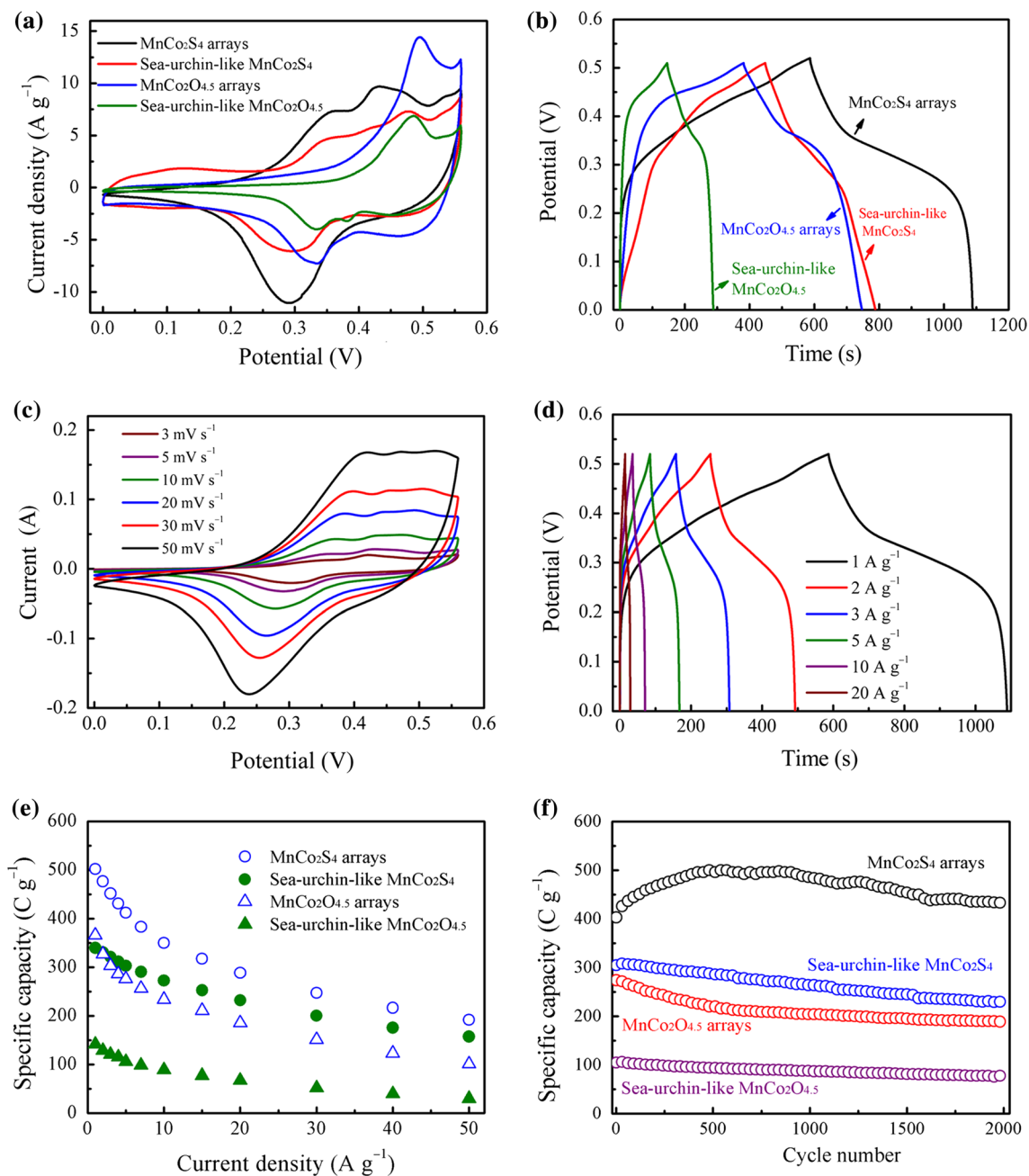
Figure 6 Electrochemical performance of the Co–Mn-based samples in a three-electrode system: **a** CV curves at 5 mV s^{-1}, **b** GCD curves at 1 A g^{-1}, **c** CV curves and **d** GCD curves at different rates of Co–Mn sulfide nanowire arrays on Ni foam, **e** specific capacity value as a function of current densities and **f** cycling performance at 5 A g^{-1} for 2000 cycles.

Mn oxide nanowire arrays and sea urchin-like Co–Mn oxide, respectively. The superior electrochemical performance can be ascribed to the structural preponderance as well as higher electrochemical activity of Co–Mn sulfide. Firstly, the Co–Mn sulfide nanowires are more porous with numerous nanosheets decorated on surface, and such attractive structure can notably increase the electroactive sites for charge storage; secondly, the Co–Mn sulfide is more electrochemically active than the Co–Mn oxide, so superior electrochemical performance has been attained for Co–Mn sulfide. With the arrays structure, the electrochemical performance of Co–Mn sulfide is considerably promoted. The Co–Mn sulfide arrays on Ni foam deliver specific capacity values of 502, 477, 452, 412, 350, 288 and 192 C g^{-1} at current densities
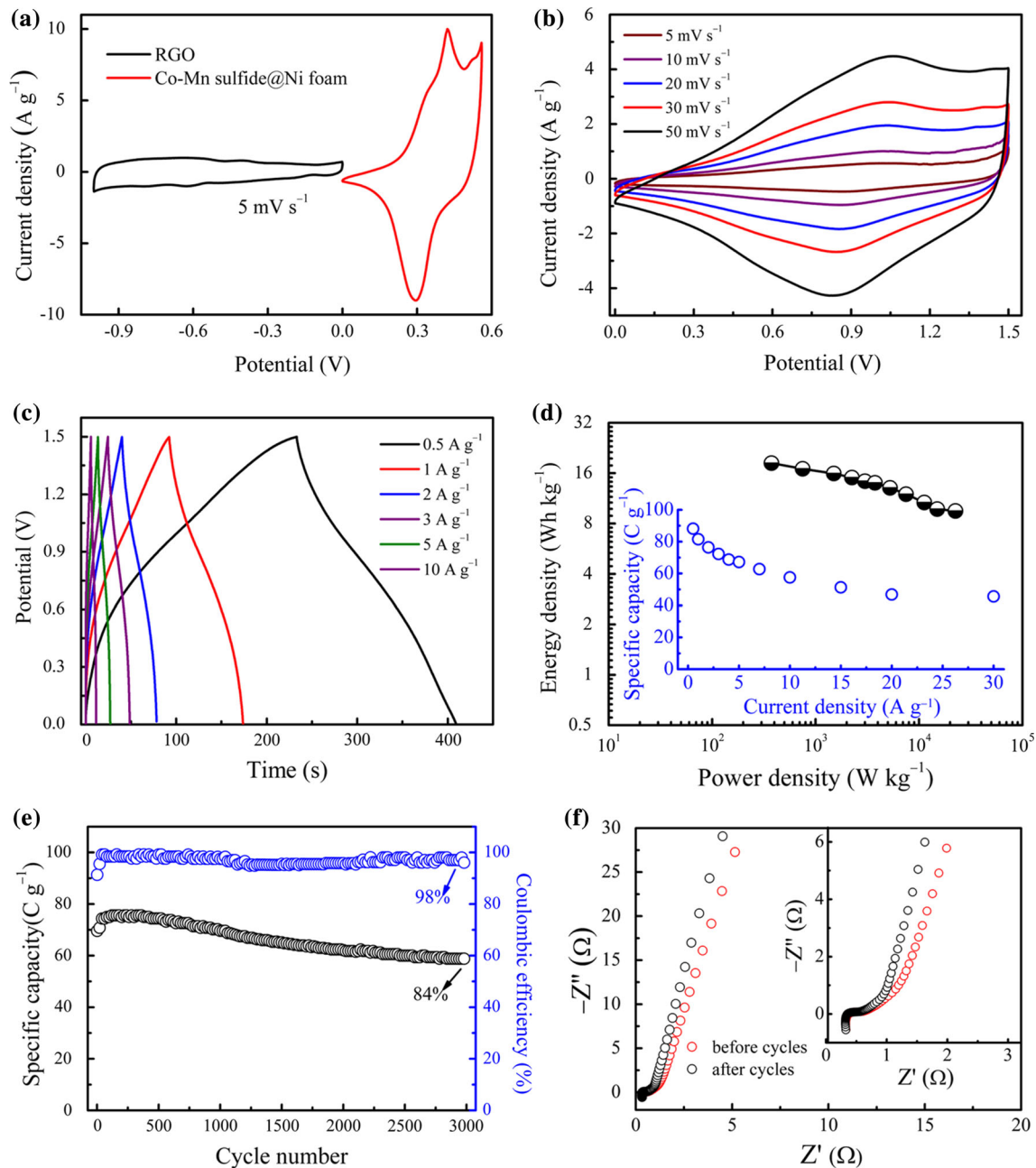
Figure 7 Electrochemical performance of Ni foam-supported Co–Mn sulfide array/RGO hybrid supercapacitor: **a** CV curves of RGO and Ni foam-supported Co–Mn sulfide arrays at a scan rate of 5 mV s^{-1} in a three-electrode system, **b** CV curves of the hybrid device at different scan rates, **c** GCD curves of the hybrid device at different current densities, **d** Ragone plot (energy density vs. power density curve) and the inset is specific capacity values at different current density of the hybrid device, **e** cycling stability and columbic efficiency of the hybrid device and **f** EIS spectra of the hybrid device before and after 3000 cycles.

of 1, 2, 3, 5, 10, 20 and 50 A g^{-1}, respectively, which are much higher than the sea urchin-like Co–Mn sulfide as well as the Co–Mn oxide samples. The cycling stability of the Co–Mn-based samples is also measured with the results shown in Fig. 6f. Obviously, the Co–Mn sulfide array sample exhibits

superior cycling stability and its specific capacity first increases from 403 to 500 C g^{-1} in the first 500 cycles and then tends to stable in the subsequent cycles. Encouragingly, 107% of the specific capacity is remained after 2000 cycles, which is much higher than Co–Mn sulfide, Co–Mn oxide nanowire arrays

on Ni foam and Co–Mn oxide samples. The sulfide experiences an erosion and recrystallization process during the long-term cycling test [22, 32, 41], resulting in the gradually variation of electroactive sites. The gradual increased specific capacity value of Ni foam-supported Co–Mn sulfide demonstrates increased electroactive sites for energy storage. The other samples all demonstrate a gradual decreased cycling performance. Therefore, the Ni foam-supported Co–Mn sulfide array sample has better ability to maintain stable electroactive sites for energy storage.

In addition, two-electrode system is also used for further investigating the electrochemical performance of Co–Mn sulfide nanowire array sample. The Co–Mn sulfide works with a potential range of 0–0.56 V and therefore used as the positive electrode. As shown in Fig. 7a, the RGO electrode works at lower potentials ranging from − 1 to 0 V, so it can be used as the negative electrode. The RGO uses the accumulation of charge and electrolyte ions on the electrode and electrolyte interface for charge storage, which is a typical material for double-electrode layer supercapacitors [42]. Therefore, the two-electrode device is a hybrid supercapacitor, which combines a battery-type positive electrode with a capacitor-type negative electrode. Owing to the different potential windows of the two electrodes in the hybrid supercapacitor, the working voltage is determined to be 1.5 V, as shown by the CV and GCD curves in Fig. 7b, c. The specific capacitance values of the hybrid cell (based on the total mass of active materials on the two electrodes) are plotted in the inset of Fig. 7d. The hybrid supercapacitor delivers a specific capacity of 88.2 C g^{-1} at a current density of 0.5 A g^{-1} and displays a high rate capability with 52% specific capacity retention as current density rising from 1 to 30 A g^{-1}. According to Eqs. 3 and 4, the energy density and power density values of the hybrid device are calculated from the GCD curves, and they are plotted into the form of Ragone plot, as shown in Fig. 7d. An energy density of 18.4 Wh kg^{-1} can be obtained at the power density of 375 W kg^{-1}. When the power density increases 60 times to 22.5 kW kg^{-1}, the energy density can still retain 9.5 Wh kg^{-1}, illustrating an ultrahigh power density. The cycling stability of the hybrid device is also evaluated by repeated GCD test at 3 A g^{-1} for 3000 cycles, which has been plotted in Fig. 7e. About 85% of the initial specific capacity as well as high coulombic efficiency of 98%

can be retained after 3000 cycles. To assess the electric impedance characteristic of the hybrid device, EIS measurements before and after cycles are also carried out, as shown in Fig. 7f. The two plots are almost overlapped except the straight line part in low frequency is more vertical, suggesting the hybrid device has excellent long-term cycling stability.

Conclusions

In summary, a facile two-step hydrothermal route was employed to synthesize Co–Mn sulfides with sea urchin-like architecture and hierarchical nanowire arrays on Ni foam. It is found that the anion-exchange sulfuration process gives rise to hierarchical structure with numerous nanosheets grown on the surface. Thusly, electroactive materials with high active areas can be harvested for the Co–Mn sulfides. Benefiting from the attractive structures and the high electrochemical activity of Co–Mn sulfides, the Co–Mn sulfides show improved performance than Co–Mn oxides with similar morphology, which exhibit superior performance in terms of high electrochemical activity and excellent cycling stability. The electrochemical performance of Co–Mn sulfide nanowire arrays sample is also evaluated by two-electrode system, and it demonstrates both high energy density and power density. Our work demonstrates that Co–Mn sulfide is a new type of electroactive materials with high electrochemical activity and the electrochemical performance can be greatly promoted by rational designing the morphology and structure of Co–Mn sulfide.

Acknowledgements

s10853-017-1976-7) contains supplementary material, which is available to authorized users.

References

[1] Simon P, Gogotsi Y (2008) Materials for electrochemical capacitors. Nat Mater 7:845–854

[2] Lu XH, Yu MH, Wang GM, Tong YX, Li Y (2014) Flexible solid-state supercapacitors: design, fabrication and applications. Energy Environ Sci 7:2160–2181

[3] Zhang LL, Zhao XS (2009) Carbon-based materials as supercapacitor electrodes. Chem Soc Rev 38:2520–2531

[4] Wang GP, Zhang L, Zhang JJ (2012) A review of electrode materials for electrochemical supercapacitors. Chem Soc Rev 41:797–828

[5] Conway BE (1999) Electrochemical supercapacitors: scientific fundamentals and technological applications. Kluwer Acaemic/Plenum Press, New York

[6] Lim E, Jo CS, Kim H, Kim MH, Mun Y, Chun J, Ye YJ, Hwang J, Ha KS, Roh KC, Kang K, Yoon S, Lee J (2015) Facile synthesis of Nb_2O_5@carbon core-shell nanocrystals with controlled crystalline structure for high-power anodes in hybrid supercapacitors. ACS Nano 9:7497–7505

[7] Wang HL, Xu ZW, Li Z, Cui K, Ding J, Kohandehghan A, Tan XH, Beniamin-Zahiri BC, Olsen CMB, Holt D Mitlin (2014) Hybrid device employing three-dimensional arrays of MnO in carbon nanosheets bridges battery-supercapacitor divide. Nano Lett 14:1987–1994

[8] Lesel BK, Ko JS, Dunn B, Tolbert SH (2016) Mesoporous $Li_xMn_2O_4$ thin film cathodes for lithium-ion pseudocapacitors. ACS Nano 10:7572–7581

[9] Elshahawy AM, Guan C, Li X, Zhang H, Hu YT, Wu HJ, Pennycook SJ, Wang J (2017) Sulfur-doped cobalt phosphide nanotube arrays for highly stable hybrid supercapacitor. Nano Energy 39:162–171

[10] Liu XY, Zhang YQ, Xia XH, Shi SJ, Lu Y, Wang XL, Gu CD, Tu JP (2013) Self-assembled porous $NiCo_2O_4$ heterostructure array for electrochemical capacitor. J Power Source 239:157–163

[11] Chen HC, Jiang JJ, Zhang L, Qi T, Xia DD, Wan HZ (2014) Facilely synthesized porous $NiCo_2O_4$ flowerlike nanostructure for high-rate supercapacitors. J Power Sources 248:28–36

[12] Guan C, Liu XM, Ren WN, Li X, Cheng CW, Wang J (2017) Rational design of metal-organic framework derived hollow $NiCo_2O_4$ arrays for flexible supercapacitor and electrocatalysis. Adv Energy Mater 7:1602391

[13] Javel MS, Zhang CL, Chen L, Xi Y, Hu CQ (2016) Hierarchical mesoporous $NiFe_2O_4$ nanocone forest directly growing on carbon textile for high performance flexible supercapacitors. J Mater Chem A 4:8851–8859

[14] Wu H, Lou Z, Yang H, Shen GZ (2015) A flexible spiral-type supercapacitor based on $ZnCo_2O_4$ nanorod electrodes. Nanoscale 7:1921–1926

[15] Sahoo S, Shim JJ (2017) Facile synthesis of three-dimensional ternary $ZnCo_2O_4$/reduced graphene oxide/NiO composite film on nickel foam for next generation supercapacitor electrodes. ACS Sustain Chem Eng 5:241–251

[16] Liu B, Liu BY, Wang QF, Wang XF, Xiang QY, Chen D, Shen GZ (2013) New energy storage option: toward $ZnCo_2O_4$ nanorods/nickel foam architectures for high-performance supercapacitors. ACS Appl Mater Interfaces 5:10011–10017

[17] Xu YN, Wang XF, An CH, Wang YJ, Jiao LF, Yuan HT (2014) Facile synthesis route of porous $MnCo_2O_4$ and $CoMn_2O_4$ nanowires and their excellent electrochemical properties in supercapacitors. J Mater Chem A 2:16480–16488

[18] Li L, He F, Gai SL, Zhang SH, Gao P, Zhang ML, Chen YJ, Yang PP (2014) Hollow structured and flower-like $C@MnCo_2O_4$ composite for high electrochemical performance in a supercapacitor. CrystEngComm 16:9873–9881

[19] Mondal AK, Su DW, Chen SQ, Ung A, Kim HS, Wang GX (2015) Mesoporous $MnCo_2O_4$ with a flake-like structure as advanced electrode materials for lithium-ion batteries and supercapacitors. Chem Eur J 21:1526–1532

[20] Chen HC, Jiang JJ, Zhang L, Wan HZ, Qi T, Xia DD (2013) Highly conductive $NiCo_2S_4$ urchin-like nanostructures for high-rate pseudocapacitors. Nanoscale 5:8879–8883

[21] Chen HC, Chen S, Fan MQ, Chao L, Chen D, Tian GL, Shu KY (2015) Bimetallic nickel cobalt selenides: a new kind of electroactive material for high-power energy storage. J Mater Chem A 3:23653–23659

[22] Chen HC, Zhang JJ, Zhao YD, Zhang L, Guo DQ, Xia DD (2015) One-pot synthesis of porous nickel cobalt sulphides: tuning the composition for superior pseudocapacitance. J Mater Chem A 3:428–437

[23] Liu XB, Wu ZP, Yin YH (2017) Hierarchical $NiCo_2S_4$@-PANI core/shell nanowires grown on carbon fiber with enhanced electrochemical performance for hybrid supercapacitors. Chem Eng J 323:330–339

[24] Chen HC, Fan MQ, Li C, Tian GL, Lv CJ, Chen D, Shu KY, Jiang JJ (2016) One-pot synthesis of hollow NiSe–CoSe nanoparticles with improved performance for hybrid supercapacitors. J Power Sources 329:314–322

[25] Zhai T, Xie S, Yu M, Fang P, Liang C, Lu X, Tong Y (2014) Oxygen vacancies enhancing capacitive properties of MnO_2 nanorods for wearable asymmetric supercapacitors. Nano Energy 8:255–263

[26] Lia ZY, Akhtar MS, Bui PTM, Yang OB (2017) Predominance of two dimensional (2D) Mn_2O_3 nanowalls thin film for high performance electrochemical supercapacitors. Chem Eng J 330:1240–1247

[27] Venkatachalam V, Alsalme A, Alghamdi A, Jayavel R (2015) High performance electrochemical capacitor based on $MnCo_2O_4$ nanostructured electrode. J Electroanal Chem 756:94–100

[28] Zhang GW, Ding F, Sang L, Wang GL, Feng MY, Ma ZP, Shao GJ (2016) Two-dimensional cobalt–manganese binary metal oxide porous nanosheets for high-performance supercapacitors. J. Solid State Electr. 20:3473–3480

[29] Peng T, Fang SL, Liu C, Hou XY, Yang HP, Luo RJ, Yu QH, Lu Y, Yan HL, Luo YS (2017) Hierarchical core–shell $CoMn_2O_4@MnO_2$ nanoneedle arrays for high-performance supercapacitors. Dalton Trans 46:7451–7456

[30] Liu MT, Fu Y, Ma HW, Wang TL, Guan C, Hu KR (2016) Flower-like manganese-cobalt oxysulfide supported on Ni foam as a novel faradaic electrode with commendable performance. Electrochim Acta 191:916–922

[31] Chen HC, Jiang JJ, Zhang L, Xia DD, Zhao YD, Guo DQ, Qi T, Wan HZ (2014) In situ growth of $NiCo_2S_4$ nanotube arrays on Ni foam for supercapacitors: maximizing utilization efficiency at high mass loading to achieve ultrahigh areal pseudocapacitance. J Power Sources 254:249–257

[32] Chen HC, Chen S, Shao HY, Li C, Fan MQ, Chen D, Tian GL, Shu KY (2016) Hierarchical $NiCo_2S_4$ nanotube @ $NiCo_2S_4$ nanosheet arrays on Ni foam for high-performance supercapacitors. Chem Asian J 11:248–255

[33] Chen S, Chen HC, Li C, Fan MQ, Lv CJ, Tian GL, Shu KY (2017) Tuning the electrochemical behavior of CoxMn3-x sulfides by varying different Co/Mn ratios in supercapacitor. J Mater Sci 52:6687–6696. https://doi.org/10.1007/s10853-017-0903-2

[34] Xia C, Alshareef HN (2015) Self-templating scheme for the synthesis of nanostructured transition-metal chalcogenide

[35] Niu LY, Wang YD, Ruan FP, Shen C, Shan S, Xu M, Sun ZK, Li C, Liu XJ, Gong YY (2016) In situ growth of $NiCo_2S_4$ @ $Ni_3V_2O_8$ on Ni foam as a binder-free electrode for asymmetric supercapacitors. J Mater Chem A 4:5669–5677

[36] Elshahawy AM, Li X, Zhang H, Hu Y, Ho KH, Guan C, Wang J (2017) Controllable $MnCo_2S_4$ nanostructures for high performance hybrid supercapacitors. J Mater Chem A 5:7494–7506

[37] Xiong SL, Chen JS, Lou XW, Zeng HC (2012) Mesoporous Co3O4 and CoO@C topotactically transformed from chrysanthemum-like Co(CO3)0.5(OH) 0.11H2O and their lithium-storage properties. Adv Funct Mater 22:861–871

[38] Chen K, Yang F, Wang G, Yin J, Cao D (2013) Facile synthesis of porous $(Co, Mn)_3O_4$ nanowires free-standing on a Ni foam and their catalytic performance for H_2O_2 electroreduction. J Mater Chem A 1:1669–1676

[39] Zhao Y, Hu LF, Zhao SY, Wu LM (2016) Preparation of $MnCo_2O_4@Ni(OH)_2$ core–shell flowers for asymmetric supercapacitor materials with ultrahigh specific capacitance. Adv Funct Mater 26:4085–4093

[40] Chen YM, Li Z, Lou XW (2015) General formation of $M_xCo_{3-x}S_4$ (M = Ni, Mn, Zn) hollow tubular structures for hybrid supercapacitors. Angew Chem Int Ed 54:10521–10524

[41] Yu JW, Wan HZ, Jiang JJ, Ruan YJ, Miao L, Zhang L, Xia DD, Xu K (2014) Activation mechanism study of dandelion-like Co_9S_8 nanotubes in supercapacitors. J Electrochem Soc 161:A996–A1000

[42] El-Kady MF, Shao YL, Kaner RB (2016) Graphene for batteries, supercapacitors and beyond. Nat Rev Mater 1:16033